

# Application Study of the Benefits for Using Silicon-Carbide Versus Silicon in Power Modules

Robert A. Wood

U.S. Army Research Laboratory  
Adelphi, MD 20783, USA  
robert.a.wood98.civ@mail.mil

Thomas E. Salem

United States Naval Academy  
Annapolis, MD 21402, USA  
salem@usna.edu

**Abstract**— On a device-level, the benefits of Silicon-Carbide (SiC) versus Silicon (Si) power components have been documented over the past several years [1-5]. The fabrication process for SiC components continues to mature and SiC products are now commercially available. The development of high-current MOSFETs and their use in all-SiC power modules have been reported [6-9]. Recently, the experimental characterization and performance of a 1200-V, 800-A all-SiC dual module has been documented [10,11]. This paper outlines the development of a simulation model for the 800-A all-SiC dual module from this experimental characterization data. Using this model, a comparison study is presented for using an all-SiC module versus an Si IGBT module in DC-DC and DC-AC power circuit applications at a 900-A, 600-A, and 300-A module level. Upgrading the power module from Si to SiC devices resulted in lower loss in nearly every simulated scenario.

## I. INTRODUCTION

Shown in Fig. 1 is one of the 1200-V, 800-A all-SiC dual modules that have been previously introduced [10,11]. The design goal for these modules was to demonstrate the feasibility for massively paralleled SiC MOSFET die to realize a high-power dual module compatible for use in a large electric vehicle traction drive. The resulting module

incorporates an integrated liquid-cooled heat sink with SiC MOSFETs and SiC JBS diodes supplied by Cree and was fabricated by Powerex based on their commercial MEGA POWER DUAL™ package [12]. The module was designed to operate at full power using a 50% by volume mixture of water and propylene glycol at an ambient temperature of 80 °C. As described in [11], one of the modules has been characterized and operated at rated conditions in an experimental full-bridge test circuit that is shown in Fig. 2.

## II. ALL-SiC POWER MODULE MODEL DEVELOPMENT

### A. Characteristic Equations

Experiments were performed on the all-SiC 800-A module to measure the following device characteristics; the MOSFET conduction voltage drop ( $V_{DS}$ ), diode forward conduction voltage drop ( $V_{SD}$ ), combined MOSFET and diode conduction voltage drop ( $V_{REV}$ ), turn-ON switching energy ( $E_{ON}$ ), turn-OFF switching energy ( $E_{OFF}$ ) and reverse recovery energy ( $E_{RR}$ ). These controlled tests were performed at various drain currents ( $I_d$ ) and device junction temperatures ( $T_j$ ) over the designed operating range. From the experimental data, a three-dimensional surface plot for each of the device characteristics as a function of  $I_d$  and  $T_j$  was generated. From these plots, a modeling function for each of the device

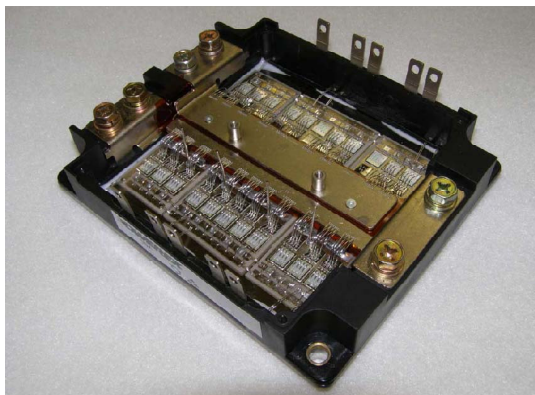


Figure 1. 1200-V, 800-A All-SiC Dual Module.

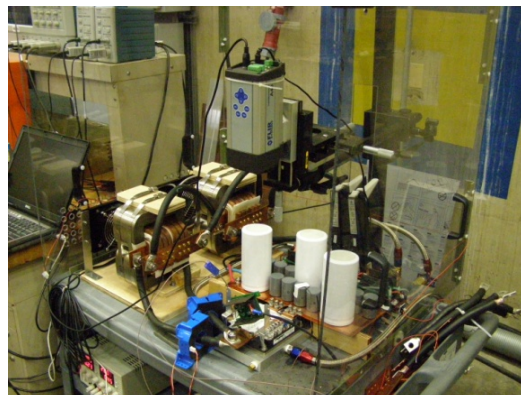


Figure 2. Experimental Full-Bridge Test Set-up.

TABLE I. VALIDATION OF TURN-ON AND TURN-OFF ENERGIES

$I_D$ (A)	$T_J$ (°C)	Measured $E_{ON}$ (mJ)	Predicted $E_{ON}$ (mJ)	Measured $E_{OFF}$ (mJ)	Predicted $E_{OFF}$ (mJ)	Error (%)
200	37.6	11.4	11.6	11.4	11.6	1.8
400	46.6	20.3	20.5	22.4	22.2	1.2
600	55.5	28.5	28.6	37.3	37.1	0.6
800	71.7	36.0	36.0	54.3	54.1	0.3
200	55.6	10.5	10.8	9.8	9.9	2.0
400	64.0	19.3	19.6	22.3	22.4	1.2
600	77.4	27.6	27.5	37.4	37.2	0.5
800	98.5	34.9	35.0	54.4	54.3	0.3
200	83.5	10.0	10.1	10.1	10.1	0.4
400	94.8	18.4	18.5	22.7	22.8	0.6
600	109	26.7	26.5	37.8	37.8	0.8
800	132	33.5	33.9	54.9	55.2	1.0
200	105	9.9	10.1	10.3	10.4	1.9
400	119	18.0	18.3	23.1	23.3	1.6
600	137	26.1	26.2	38.5	38.7	0.5

characteristics ( $X_i$ ) was developed of the form:

$$X_i(I_d, T_j) = (\alpha_{1,i}I_d^2 + \beta_{1,i}I_d + \gamma_{1,i})T_j^2 + (\alpha_{2,i}I_d^2 + \beta_{2,i}I_d + \gamma_{2,i})T_j + (\alpha_{3,i}I_d^2 + \beta_{3,i}I_d + \gamma_{3,i}) \quad (1)$$

For example, Table I summarizes the experimental (measured) and simulated (predicted) results for  $E_{ON}$  and  $E_{OFF}$  for several experimental data combinations of  $I_d$  and  $T_j$  using the equations developed for  $E_{ON}$  and  $E_{OFF}$ . Also shown in the table is the error from the predicted and measured values. In the case of  $E_{ON}$  and  $E_{OFF}$ , the maximum error over the entire measured range was 5%. This demonstrates good accuracy of the modeling equation to predict the measured switching energies. For the other characteristics, the maximum error was 8%, 2%, 11%, and 13% for the  $V_{DS}$ ,  $V_{SD}$ ,  $V_{REV}$  and  $E_{RR}$  characteristics, respectively. Each device characteristic equation was linearly normalized to a single device.

#### B. 900-A, 600-A, and 300-A All-SiC Modules

Previous work had reported on the characterization of an all-SiC dual module that contained two parallel configurations of ten 80-A MOSFETs and ten 50-A JBS diodes [10,11]. For this study, it was desired to have an all-SiC module to compare to an IGBT at standard commercial current ratings of 900-A, 600-A, and 300-A. The comparison will be the most valid at the 900-A level as the experimental data is based on an 800-A module operating in the same physical package as a commercial 900-A Si module.

To develop a module model at each current level, an integer number of SiC die were chosen to get as close to the Si current rating as possible. Thus, eleven die were chosen for the 900-A module, eight for the 600-A module and four for the 300-A module, which are all within 10% of the Si rating. The all-SiC modules rated at 880-A, 640-A and 320-A

TABLE II. ALL-SiC MODULE CHARACTERISTICS

Part Name	80-A Die	$E_{ON}$ (mJ) <sup>a</sup>	$E_{OFF}$ (mJ) <sup>a</sup>	$E_{RR}$ (mJ) <sup>a</sup>	$V_{DS}$ (V) <sup>a</sup>	$V_{SD}$ (V) <sup>a</sup>	$V_{REV}$ (V) <sup>a</sup>
SiC-900	11	34.8	56.7	3.65	2.45	2.34	1.27
SiC-600	8	32.0	50.6	3.34	2.20	2.22	1.21
SiC-300	4	32.0	50.6	3.34	2.20	2.22	1.21

a. All characteristics are at the rated current and  $T_j$  of 125°C

hereafter will be referred to as SiC-900, SiC-600 and SiC-300 respectively. Table II shows the characteristics for the SiC modules at a die temperature of 125°C and the rated currents of 900-A, 600-A and 300-A.

Some characteristics are not influenced by physical packaging such as  $V_{DS}$ ,  $V_{SD}$  and  $V_{REV}$ . Rather, these characteristics largely dependent on the number of die within the module. Therefore, it is accurate to linearly approximate these characteristics the modules based on the number of devices. For instance, a module containing one MOSFET conducting 10 A would have virtually the same  $V_{DS}$  as a module containing two MOSFETs conducting 20 A.

However, the switching characteristics in the modules ( $E_{ON}$ ,  $E_{OFF}$  and  $E_{RR}$ ) do depend significantly on the parasitics of the packaging [13,14]. Therefore, these characteristics will not precisely scale linearly from a 900-A package to a 300-A package. Since a 300-A SiC module has not been characterized, the switching energy was simply scaled linearly. Switching characteristics will be correct for the 900-A range as the basis module was a 900-A package, but will be less accurate for the 600 and 300-A parts. A future study will be conducted to more precisely characterize the switching energies of a 300-A module.

As previously mentioned, the 800-A all-SiC module that was characterized included a high-performance integrated liquid-cooled heatsink for enhanced capabilities. Since the commercially available Si parts don't contain this type of heatsink, the published thermal resistance of the Si devices was used for the SiC modeling.

### III. SILICON MODULE SELECTION

Datasheets from several manufacturers were reviewed to select the Si modules for the comparison study. To be considered, the datasheet had to include enough information to accurately develop a model from the similar device characteristics for the module. These characteristics were evaluated to assess the modules:  $E_{ON}$ ,  $E_{OFF}$ , IGBT saturation voltage at the rated current ( $V_{CE}$ ), and thermal resistance ( $R_{TH}$ ). The Si IGBT's  $V_{CE}$  is a comparable characteristic to the SiC MOSFET's  $V_{DS}$ . At each of the three separate current ratings, device characteristics at a die temperature of 125°C were used. The potential rise in die temperature ( $\Delta T_j$ ) of the IGBT switching a 20 kHz, 50 % duty cycle square wave at the rated current ( $I_R$ ) was estimated using (2).

$$\Delta T_j = ((E_{ON} + E_{OFF}) 20 \text{ kHz} + (50 \%) V_{CE} \cdot I_R) R_{TH} \quad (2)$$

Equation (2) approximates the circuit performance and favors the modules with either the lowest losses or the lowest thermal resistance. From among the available Si parts, the

TABLE III. SILICON SWITCHES CONSIDERED FOR COMPARISON

Company	Part No.	$E_{ON}$ (mJ) <sup>a</sup>	$E_{OFF}$ (mJ) <sup>a</sup>	$V_{CE}$ (V) <sup>a</sup>	$R_{TH}$ (°C/W)	$\Delta T_J$ (°C)
<b>900-A Modules</b>						
Powerex	CM900DU-24NF [15]	68	142	2.0	0.021	107
Infineon	FF900R12IP4 [16]	100	160	2.0	0.030	180
<b>600-A Modules</b>						
Powerex	CM600DY-24A [17]	103	64	2.4	0.034	138
Eupec	FF600R12KL4C [18]	100	90	2.4	0.032	145
Powerex	MG600Q2YS60A [19]	130	130	3.2	0.029	179
Infineon	FF600R12IP4 [20]	77	105	2.0	0.045	191
Eupec	FF600R12KE3 [21]	120	95	2.0	0.044	216
Powerex	CM600DU-24NFH [22]	264	254	5.0	0.034	403
<b>300-A Modules</b>						
Powerex	CM300DU-24NFH [23]	13.4	10.2	5.0	0.066	81
Powerex	MG300Q2YS60A [24]	54.0	52.7	2.8	0.044	115
Powerex	CM300DY-24A [25]	38.0	32.8	2.4	0.066	117
Infineon	FF300R12KT3 [26]	25.0	37.0	1.9	0.085	130
SemiKron	SKM300GB12V [27]	11.3	31.6	2.3	0.110	132
Microsemi	APGTGT300A120G [28]	30.0	30.0	2.0	0.090	135
Infineon	FF300R12KE3 [29]	25.0	44.0	2.0	0.085	143
SemiKron	SKM300GM12T4 [30]	26.2	29.2	2.3	0.110	159
IXYS	MII300-12A4 [31]	48.5	41.4	3.1	0.090	203

a.  $E_{ON}$ ,  $E_{OFF}$  and  $V_{CE}$  are listed at  $T_J$  of 150°C for the SemiKron parts and 125°C for all other modules.

two modules with the lowest estimated die temperature at each current level were chosen for comparison with the all-SiC modules. Note that the size of the module, which would affect the power density of the system, was not considered as a selection parameter.

#### A. 900-A Module Selection

As shown in Table III, only 2 modules at the 900-A rating were found at the time of publication. These modules, Powerex's CM900DU-24NF and Infineon's FF900R12IP4 were used for the comparison, and hereafter are referred to as Si-900-1 and Si-900-2, respectively. Notice that the Si-900-1 and Si-900-2 module shave more than double the amount of  $E_{ON}$  and  $E_{OFF}$  than the SiC-900. However, the SiC-900 has 25% more forward drop than the Si parts. Therefore, it was expected that the SiC module would perform better at higher frequencies where switching loss dominates.

#### B. 600-A Module Selection

Six 600-A silicon modules were considered for comparison and the resulting characteristics of each are also shown in Table III. Of these modules, Powerex's CM600DY-24A and Eupec's FF600R12KL4C had the lowest calculated  $\Delta T_J$  and were therefore selected. These modules hereafter will be referred to as Si-600-1 and Si-600-2, respectively. Both

modules had comparably low  $E_{ON}$ ,  $E_{OFF}$  and  $R_{TH}$  characteristics which resulted in the lowest  $\Delta T_J$ . In comparison, the SiC-600 module listed in Table II had lower  $V_{DS}$ ,  $E_{ON}$  and  $E_{OFF}$  and therefore was expected to have less loss than both 600-A Si modules.

#### C. 300-A Module Selection

Nine 300-A modules were considered for comparison and the device characteristics are shown in Table III. As can be seen from the table, the devices with the lowest anticipated  $\Delta T_J$  are Powerex's CM300DU-24NFH and MG300Q2YS60A. From this point forward these modules will be referred to as Si-300-1 and Si-300-2, respectively. Although Si-300-1 had the highest  $V_{CE}$ , the low  $R_{TH}$ ,  $E_{ON}$  and  $E_{OFF}$  resulted in the lowest  $\Delta T_J$ . Conversely, Si-300-2 had the highest  $E_{ON}$  and  $E_{OFF}$  but the lowest  $R_{TH}$  and therefore the second lowest  $\Delta T_J$ . Comparing with the SiC-300 module listed in Table II, several distinct differences between the modules at the 300-A level are evident. First, the Si-300-1 module had the lowest  $E_{ON}$  and  $E_{OFF}$  but the highest  $V_{CE}$ . Second, the SiC-300 module had the lowest  $V_{DS}$ . And lastly, Si-300-2 had the highest  $E_{ON}$  and  $E_{OFF}$ . At high switching frequencies, the Si-300-1 module will have an advantage while at lower frequencies the SiC-300 module would have the advantage.

### IV. SIMULATION APPROACH

Two simulations were performed at each current level: DC-DC conversion via a traditional Buck converter operating in continuous current mode (CCM) and a DC-AC inverter operating a motor load at an AC frequency of 120 Hz. The desired system platform for the converters was chosen to be a vehicle. This determined the voltage and the coolant temperature values. The high side voltage for both converter and inverter was chosen at a typical vehicle voltage of 600 V, and the thermal ambient was selected as 100°C.

Since the parameters for the Si modules are typically given at only two temperatures (25°C and 125°C), insufficient data was available to develop temperature dependent models. Therefore, the amount of current produced at each switching frequency was adjusted to yield a constant  $T_J$  of 125°C. The datasheet characteristics of the module were applicable in this condition since all modules included data at a  $T_J$  of 125°C. For comparison, the all-SiC module was operated at the same current level with the  $T_J$  at that operating point calculated. The thermal resistance of the Si module was used for the thermal resistance of the SiC module to eliminate the variability of this parameter.

#### A. DC-DC Converter

Most DC-DC converters have similar semiconductor current waveforms. For this simulation, a waveform was created to represent a typical buck converter operating in CCM using a dual module that contains an upper switch and parallel diode ( $Q_1$ ) and a lower switch and diode ( $Q_2$ ). This waveform is shown in Fig. 3 in which the switch of  $Q_1$  turns ON at a non-zero current resulting in a turn ON energy  $E_{ON}$ . Current increased as the inductor was energized and then  $Q_1$  was turned OFF, resulting in an  $E_{OFF}$ . The amount of ON time was set to 50% of the switching period. At switch transition, the diode in  $Q_2$  conducted the current until the  $Q_1$  switch

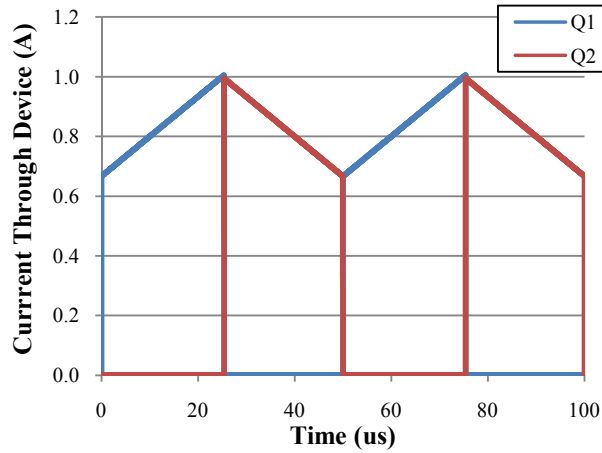


Figure 3. Example DC-DC Converter Device Currents.

turned ON. In Fig. 3, the switching frequency was 20 kHz and the peak current was 1.0 A. For each evaluated switching frequency, the peak current was increased until the Si  $T_J$  was 125°C. The losses in  $Q_1$  and  $Q_2$  were summed to determine the total module losses in the DC-DC converter.

#### B. DC-AC Inverter

Current waveforms for a typical space vector modulation controlled three-phase DC-AC inverter with a motor load are common and well-documented [32]. For this study, a three-phase inverter utilizing three dual modules was examined. Fig. 4 displays a sample section of the current waveform for one dual module in a three-phase inverter operating at a 20 kHz switching frequency. For the DC-AC inverter study, the switching frequency was varied between 4 to 20 kHz while the output AC frequency was maintained at 120 Hz. Again, the peak current for each simulation was increased until the Si  $T_J$  was 125°C. The losses generated for each dual module were summed to determine a total DC-AC inverter module loss.

### V. RESULTS

#### A. 900-A Modules

As the switching frequency of DC-DC converter and the

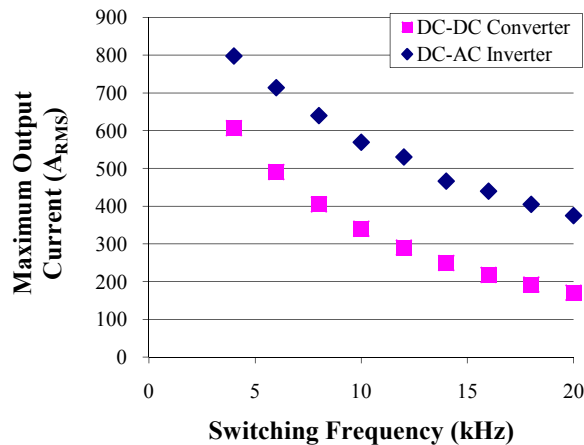


Figure 5. Si-900-1 Maximum Current.

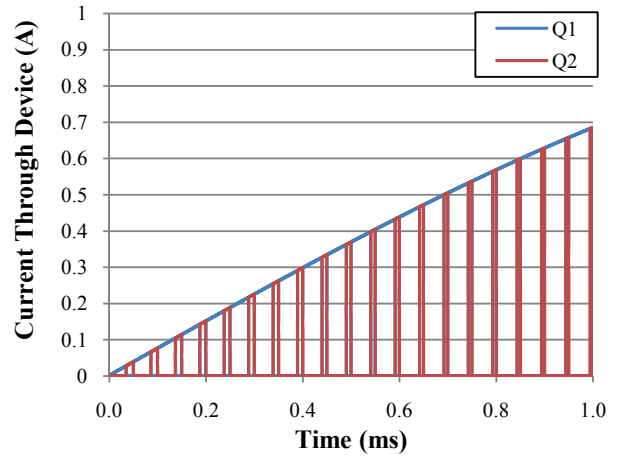


Figure 4. Example DC-AC Inverter Device Currents.

DC-AC inverter increased, the peak current of the module decreased as more of the losses in the module resulted from switching loss. For example, as shown in Fig. 5, at the lowest switching frequency the Si-900-1 module was capable of 607  $A_{RMS}$  and 798  $A_{RMS}$  in the DC-DC converter and the DC-AC inverter, respectively. However, this module was only capable of producing 170  $A_{RMS}$  and 375  $A_{RMS}$  at a switching frequency of 20 kHz.

The simulation for SiC module was performed at the same maximum current level as each Si module. Fig. 6 shows the amount of loss for the DC-DC converter and for the three-phase DC-AC inverter for Si-900-1 and SiC-900. As can be seen from the figure, the module loss in both the DC-DC converter and the DC-AC inverter was always higher for the Si-900-1 module than the SiC-900 module. This reduction in loss increased at higher switching frequencies because the SiC-900 module had lower  $E_{ON}$  and  $E_{OFF}$ . For the DC-DC converter, module loss was reduced 47 and 76% for the 4 and 20 kHz switching frequencies, respectively. While the loss in the DC-AC inverter was reduced 13% at 4 kHz and 66% at 20 kHz. This benefit resulted solely from upgrading the semiconductor devices from Si to SiC in the module.

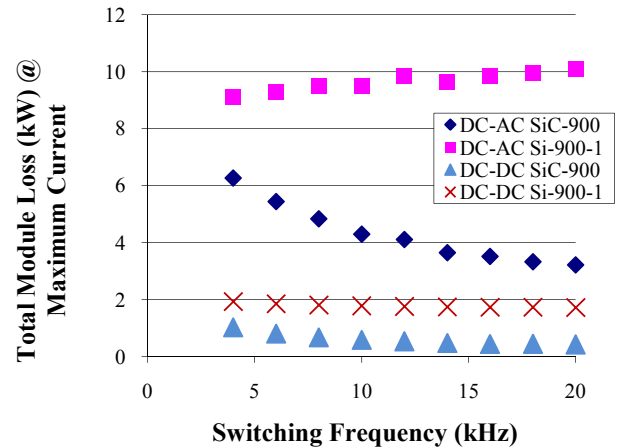


Figure 6. Total Module Loss for Si-900-1 and SiC-900.

TABLE IV. 900-A SWITCH SIMULATION RESULTS

Si-900-1 vs SiC-900							Si-900-2 vs. SiC-900					
$F_{SW}$ (kHz)	$I_{RMS}$ (A <sub>RMS</sub> )	$P_{TOT}$ (kW)	IGBT $T_J$ (°C)	$P_{TOT}$ (kW)	MOS $T_J$ (°C)	Loss Red (%)	$I_{RMS}$ (A <sub>RMS</sub> )	$P_{TOT}$ (kW)	IGBT $T_J$ (°C)	$P_{TOT}$ (kW)	MOS $T_J$ (°C)	Loss Red (%)
DC-DC Converter Simulation												
4	607	1.93	125.0	1.03	115.2	47	412	1.26	125.0	0.53	110.9	58
8	405	1.81	125.0	0.68	110.9	63	211	1.15	125.0	0.27	106.3	77
12	290	1.76	125.0	0.53	109.1	70	108	1.11	125.0	0.17	104.2	85
16	218	1.74	125.0	0.45	108.2	74	47	1.09	125.0	0.10	102.6	91
20	170	1.73	125.0	0.42	107.6	76	8	1.07	125.0	0.04	101.2	96
DC-AC Inverter Simulation												
4	798	9.12	125.0	6.26	121.1	31	562	6.40	125.0	3.25	115.3	49
8	640	9.47	125.0	4.84	116.1	49	397	6.50	125.0	2.21	110.4	66
12	530	9.85	125.0	4.11	113.5	58	293	6.73	125.0	1.74	108.0	74
16	440	9.86	125.0	3.51	111.7	64	210	6.59	125.0	1.33	106.2	80
20	375	10.11	125.0	3.22	110.6	68	153	6.66	125.0	1.12	105.1	83

The rest of the simulation data at the 900-A modules is show in Table IV. In the table,  $I_{RMS}$  is the RMS current of the output current;  $P_{TOT}$  is the total module loss; IGBT  $T_J$  is the maximum Si IGBT temperature; MOS  $T_J$  is the maximum SiC MOSFET temperature; and Loss Red is the reduction in loss that results from replacing the Si module components with SiC.

The data in Table IV shows that at a 900-A module level, there are significant benefits achieved by using SiC technology over traditional Si components for all frequencies simulated for both the DC-DC converter and the DC-AC inverter. This was anticipated as the SiC-900 module had lower  $E_{ON}$  and  $E_{OFF}$  than both Si-900 modules. If the Si-900-2 module was upgraded with SiC, loss would be reduced in the DC-DC converter 58% at 4 kHz and 96% at 20 kHz, or reduced in the DC-AC inverter 49% at 4 kHz and 83% at 20 kHz. Additionally, while the IGBTs in the Si modules were at a  $T_J$  of 125°C, the maximum MOSFET  $T_J$  was lower at all operating conditions which will improve reliability.

#### B. 600-A Modules

Next, the 600-A modules were simulated and the results are summarized in Table V. Notice from the table, that similar to the 900-A level, the SiC module at the 600-A level was always more efficient than either of the Si modules. If the devices in the Si-600-1 module were upgraded to SiC, loss was reduced 50% at 4 kHz and 66% at 20 kHz for the DC-DC converter, or reduced 41% at 4 kHz and 63% at 20 kHz for the

DC-AC inverter. Likewise, if the Si-600-2 devices were upgraded with SiC, loss would be reduced 48% at 4 kHz and 81% at 20 kHz for the DC-DC converter, or 43% at 4 kHz and 67% at 20 kHz for the DC-AC inverter. Also, while the Si IGBTs had a  $T_J$  of 125°C, the maximum SiC MOSFET  $T_J$  was lower at all operating conditions. Therefore, upgrading either Si module will lower the module loss, decrease  $T_J$ , and increase the reliability of the module.

#### C. 300-A Modules

Lastly, the 300-A modules were simulated and the results are summarized in Table VI. As seen from the table, the 300-SiC module was more efficient than the Si modules in all cases except for the comparison with the Si-300-1 module operating at 20 kHz. The lower  $E_{ON}$  and  $E_{OFF}$  of Si-300-1 module provided a significant benefit at higher switching frequencies and therefore the module had lower loss at the highest frequency than the SiC-300 module. However, if the Si-300-1 module's devices were upgraded with SiC, loss decreased 37% at 4 kHz and increased 1% at 20 kHz for the DC-DC converter, or reduced 31% at 4 kHz and 5% at 20 kHz for the DC-AC inverter. If the Si-300-2 devices were upgraded with SiC, loss reduced 31% at 4 kHz and 47% at 20 kHz for the DC-DC converter, or reduced 25% at 4 kHz and 39% at 20 kHz for the DC-AC inverter.

In the 300-A simulation data, some conditions increased the SiC MOSFET  $T_J$  above 125°C. One reason for this increase was the capability of a MOSFET to bi-directionally

TABLE V. 600-A SWITCH SIMULATION RESULTS

Si-600-1 vs SiC-600							Si-600-2 vs. SiC-600					
$F_{SW}$ (kHz)	$I_{RMS}$ (A <sub>RMS</sub> )	$P_{TOT}$ (kW)	IGBT $T_J$ (°C)	$P_{TOT}$ (kW)	MOS $T_J$ (°C)	Loss Red (%)	$I_{RMS}$ (A <sub>RMS</sub> )	$P_{TOT}$ (kW)	IGBT $T_J$ (°C)	$P_{TOT}$ (kW)	MOS $T_J$ (°C)	Loss Red (%)
DC-DC Converter Simulation												
4	358	1.15	125.0	0.58	114.2	50	363	1.13	125.0	0.59	113.6	48
8	236	1.04	125.0	0.42	111.6	59	241	1.09	125.0	0.44	111.3	60
12	168	0.99	125.0	0.36	110.7	64	163	1.09	125.0	0.35	109.6	68
16	127	0.97	125.0	0.34	110.1	65	108	1.10	125.0	0.29	108.0	74
20	101	0.97	125.0	0.32	109.8	66	67	1.13	125.0	0.22	106.2	81
DC-AC Inverter Simulation												
4	451	5.34	125.0	3.14	117.0	41	452	5.55	125.0	3.15	116.0	43
8	353	5.36	125.0	2.59	114.0	52	359	5.70	125.0	2.65	113.5	53
12	288	5.47	125.0	2.34	112.4	57	297	5.96	125.0	2.44	112.2	59
16	237	5.40	125.0	2.11	111.5	61	244	6.00	125.0	2.19	111.2	63
20	200	5.48	125.0	2.03	110.9	63	203	6.18	125.0	2.06	110.4	67

TABLE VI. 300-A SWITCH SIMULATION RESULTS

Si-300-1 vs SiC-300							Si-300-2 vs. SiC-300					
$F_{SW}$ (kHz)	$I_{RMS}$ (A <sub>RMS</sub> )	$P_{TOT}$ (kW)	IGBT $T_J$ (°C)	$P_{TOT}$ (kW)	MOS $T_J$ (°C)	Loss Red (%)	$I_{RMS}$ (A <sub>RMS</sub> )	$P_{TOT}$ (kW)	IGBT $T_J$ (°C)	$P_{TOT}$ (kW)	MOS $T_J$ (°C)	Loss Red (%)
DC-DC Converter Simulation												
4	179	0.62	125.0	0.39	120.4	37	221	0.79	125.0	0.54	118.7	31
8	161	0.66	125.0	0.52	129.5	22	152	0.74	125.0	0.48	118.0	35
12	145	0.70	125.0	0.63	136.8	11	109	0.72	125.0	0.43	117.2	40
16	130	0.73	125.0	0.70	142.3	3	81	0.71	125.0	0.40	116.1	44
20	117	0.75	125.0	0.76	146.6	-1	60	0.70	125.0	0.37	114.8	47
DC-AC Inverter Simulation												
4	213	2.84	125.0	1.96	120.5	31	273	3.90	125.0	2.92	120.5	25
8	203	3.08	125.0	2.43	125.6	21	220	3.94	125.0	2.73	119.1	31
12	193	3.31	125.0	2.87	129.7	13	184	4.06	125.0	2.67	118.4	34
16	181	3.49	125.0	3.15	133.4	10	153	4.01	125.0	2.52	117.8	37
20	172	3.69	125.0	3.51	136.8	5	131	4.09	125.0	2.49	117.4	39

conduct current, whereas an IGBT cannot. Therefore, the SiC MOSFET conducted more current throughout and therefore had a higher  $T_J$ . This property allowed for reduced loss in the DC-DC converter as the MOSFET was more efficient at than the parallel diode. Even at the 300-A level, upgrading with SiC would lower the loss in almost all of the simulated conditions and demonstrates the benefit of utilizing SiC technology. Additional research is required to determine the actual  $E_{ON}$ ,  $E_{OFF}$  and  $E_{RR}$  of a 300-SiC module, which should be lower than the estimated linear projections used in this paper.

## VI. CONCLUSION

This paper details the creation of a set of equations that describe the characteristics of a SiC module containing varying amounts of 80-A SiC MOSFET die. These equations are based on experimental data characterizing an 800-A all-SiC dual module. These equations were used to compare SiC modules to state of the art Si IGBT commercial modules at three different current levels. Two commercially available Si IGBT modules at a 900-A, 600-A and 300-A level were compared to an equivalently rated SiC module.

At the 900-A level, where the analysis was most accurate, loss could be reduced at least 47% at 4 kHz and 76% at 20 kHz in a DC-DC converter by upgrading the Si devices with SiC. Loss could be reduced at least 31% at a switching frequency of 4 kHz and 68% at 20 kHz for the DC-AC inverter by upgrading the Si devices with SiC. In all simulation conditions, SiC produced lower module losses, and reduced junction temperatures which would improve module reliability.

At the 600-A level, loss could be reduced at least 50% at 4 kHz and 66% at 20 kHz in a DC-DC converter by upgrading the Si devices with SiC. Loss could be reduced at least 41% at a switching frequency of 4 kHz and 63% at 20 kHz for the DC-AC inverter by upgrading the Si devices with SiC. Again, utilizing SiC produced lower module losses, and reduced junction temperatures which would improve module reliability.

At the 300-A module level, where the analysis is least accurate, the SiC module still outperformed the Si modules. Accuracy was reduced because this work linearly scaled the dynamic module characteristics  $E_{ON}$ ,  $E_{OFF}$  and  $E_{RR}$  without

accounting for their dependency on package parasitics. Actual  $E_{ON}$ ,  $E_{OFF}$  and  $E_{RR}$  should be even lower for a packaged 300-A All-SiC dual module. Yet in this comparison, loss decreased at least 37% at a switching frequency of 4 kHz but only increased 1% at 20 kHz for the DC-DC converter, by upgrading the Si devices to SiC. Similarly, loss decreased 31% at a switching frequency of 4 kHz and 5% at 20 kHz for a DC-AC inverter.

At each current level it was shown that upgrading Si IGBTs with equally-rated SiC MOSFETs could make both a DC-DC converter and a DC-AC inverter significantly more efficient. As a result, the system designer has two distinct engineering paths. First, they can take advantage of the efficiency increase by decreasing the demands and size of the system cooling. This has the additional benefit of operating the power electronics at a lower temperature which yields higher system reliability. The second approach is to increase the switching frequency of the power electronics which directly reduces the size of associated passive components. This would increase the module loss, but is a trade-off against size reduction. Additionally, as the technology of SiC devices continue to mature, the promise of operating at  $T_J$  of 200°C and above will be realized.

## REFERENCES

- [1] G. A. Elasser and T.P. Chow, T.P., "Silicon carbide benefits and advantages for power electronics circuits and systems," Proceedings of the IEEE, vol. 90, issue 6, 2002, pp. 969-986.
- [2] J. Richmond, S.H. Ryu, M. Das, S. Krishnaswami, S. Hodge Jr., A. Agarwal, and J. Palmour, "An overview of Cree silicon carbide power devices," Power Electronics in Transportation, 2004, pp. 37-42.
- [3] P. Friedrichs, "Silicon carbide power semiconductors — new opportunities for high efficiency," 3rd IEEE Conference on Industrial Electronics and Applications, 2008, pp. 1770-1774.
- [4] T. Kimoto, "SiC technologies for future energy electronics," 2010 Symposium on VLSI Technology, 2010, pp. 9-14.
- [5] S. Sandeep and R. Komaragiri, "Simulation and comparison studies of Silicon Carbide and silicon power devices," 2010 India International Conference on Power Electronics, 2011, pp. 1-5.
- [6] T.E. Salem, D.P. Urciuoli, R. Green, and G.K. Ovrebø, "High-temperature high-power operation of a 100 A SiC DMOSFET module," 24th Annual IEEE Applied Power Electronics Conference and Exposition, Feb. 2009, pp. 653-657.
- [7] R.A. Wood, D.P. Urciuoli, T.E. Salem, and R. Green, "Reverse conduction of a 100 A SiC DMOSFET module in high-power

- applications,” 25th Annual IEEE Applied Power Electronics Conference and Exposition, Feb. 2010, pp. 1568-1571.
- [8] D. Urciuoli, R. Green, A. Lelis, and D. Ibitayo, “Performance of a dual, 1200 V, 400 A, silicon-carbide power MOSFET module,” 2010 IEEE Energy Conversion Congress and Exposition, 2010, pp. 3303-3310.
  - [9] D. Grider, M. Das, A. Agarwal, J. Palmour, S. Leslie, J. Ostop, R. Raju, M. Schutten, and A. Hefner, “10 kV/120 A SiC DMOSFET half H-bridge power modules for 1 MVA solid state power substation,” 2011 IEEE Electric Ship Technologies Symposium, 2011, pp. 131-134.
  - [10] R. Wood and T. E. Salem, “Characteristics of a 1200 V, 550 A SiC DMOSFET dual module,” Proceedings PCIM, May 2010, pp. 293-298.
  - [11] R. Wood and T. E. Salem, “Evaluation of a 1200 V, 800 A All SiC Dual Module”, IEEE Transactions on Power Electronics, Vol. PP, Issue 99, 2011.
  - [12] J. Yamada, Y. Yu, J. F. Donlon, and E. R. Motto, “New MEGA POWER DUAL IGBT module with advanced 1200 V CSTBT chip,” Proceedings of the 37th Annual IEEE Industry Applications Conference, Oct. 2002, pp. 2159-2164.
  - [13] M. Frisch, T. Emo, “Power Module with Additional Low Inductive Current Path,” 2010 6th International Conference on Integrated Power Electronics Systems (CIPS), 2010, Page(s): 1-6.
  - [14] L.D. Stevanovic, R.A. Beaupre, E.C. Delgado, and A.V. Gowda, “Low Inductance Power Module with Blade Connector,” 2010 Twenty-Fifth Annual IEEE Applied Power Electronics Conference and Exposition (APEC), Feb. 2010, pp.1603-1609.
  - [15] Datasheet for CM900DU-24NF, 02/10 Rev. 1. Retrieved from [http://www.pwr.com/pwr/docs/cm900du\\_24nf.pdf](http://www.pwr.com/pwr/docs/cm900du_24nf.pdf).
  - [16] Datasheet for FF900R12IP4, 2009-08-13 Rev. 2.4. Retrieved from [http://www.infineon.com/dgdl/DS\\_FF900R12IP4\\_2\\_4.PDF?folderId=db3a304412b407950112b4095b0601e3&fileId=db3a30431f848401011f8bb861df3edd](http://www.infineon.com/dgdl/DS_FF900R12IP4_2_4.PDF?folderId=db3a304412b407950112b4095b0601e3&fileId=db3a30431f848401011f8bb861df3edd).
  - [17] Datasheet for CM600DY-24A, Rev. 11/07. Retrieved from [http://www.pwr.com/pwr/docs/cm600dy\\_24a.pdf](http://www.pwr.com/pwr/docs/cm600dy_24a.pdf).
  - [18] Datasheet for FF600R12KL4C, 02.09.1999, Rev. 2. Retrieved from <http://www.infineon.com/dgdl/ff600r12kl4c.pdf?folderId=db3a304412b407950112b4095b0601e3&fileId=db3a304412b407950112b433aeb95d2d>.
  - [19] Datasheet for MG600Q2YS60A, 07/05. Retrieved from <http://www.pwr.com/pwr/docs/mg600q2ys60a.pdf>.
  - [20] Datasheet for FF600R12IP4, 2009-08-13, Rev. 2.4. Retrieved from [http://www.infineon.com/dgdl/DS\\_FF600R12IP4\\_2\\_4.PDF?folderId=db3a304412b407950112b4095b0601e3&fileId=db3a30431f848401011f8b94350f3eb9](http://www.infineon.com/dgdl/DS_FF600R12IP4_2_4.PDF?folderId=db3a304412b407950112b4095b0601e3&fileId=db3a30431f848401011f8b94350f3eb9).
  - [21] Datasheet for FF600R12KE3, 2002-07-30, Rev. 2.0. Retrieved from [http://www.infineon.com/dgdl/db\\_ff600r12ke3.pdf?folderId=db3a304412b407950112b4095b0601e3&fileId=db3a304412b407950112b433b8295d55](http://www.infineon.com/dgdl/db_ff600r12ke3.pdf?folderId=db3a304412b407950112b4095b0601e3&fileId=db3a304412b407950112b433b8295d55).
  - [22] Datasheet for CM600DU-24NFH, 07/11 Rev. 2. Retrieved from <http://www.pwr.com/pwr/docs/cm600du-24nfh.pdf>.
  - [23] Datasheet for CM300DU-24NFH, 07/11 Rev. 1. Retrieved from <http://www.pwr.com/pwr/docs/cm300du-24nfh.pdf>.
  - [24] Datasheet for MG300Q2YS60A, 5/05. Retrieved from <http://www.pwr.com/pwr/docs/mg300q2ys60a.pdf>.
  - [25] Datasheet for CM300DY-24A, 10/10 Rev. 1. Retrieved from [http://www.pwr.com/pwr/docs/cm300dy\\_24a.pdf](http://www.pwr.com/pwr/docs/cm300dy_24a.pdf).
  - [26] Datasheet for FF300R12KT3, 2007-10-19, Rev. 3.0. Retrieved from [http://www.infineon.com/dgdl/DS\\_FF300R12KT3\\_3\\_0.PDF?folderId=db3a304412b407950112b4095b0601e3&fileId=db3a304412b407950112b4345e3e6019](http://www.infineon.com/dgdl/DS_FF300R12KT3_3_0.PDF?folderId=db3a304412b407950112b4095b0601e3&fileId=db3a304412b407950112b4345e3e6019).
  - [27] Datasheet for SKM300GB12V, Rev. 5 - 23.03.2011. Retrieved from [http://www.semikron.com/products/data/cur/assets/SKM300GB12V\\_22892073.pdf](http://www.semikron.com/products/data/cur/assets/SKM300GB12V_22892073.pdf).
  - [28] Datasheet for APTGT300A120G, Rev 1, July 2006. Retrieved from <http://www.microsemi.com/en/sites/default/files/datasheets/APTGT300A120G-Rev1.pdf>.
  - [29] Datasheet for FF300R12KE3, 2007-06-27, Rev. 3.2. Retrieved from [http://www.infineon.com/dgdl/DS\\_FF300R12KE3\\_3\\_2.PDF?folderId=db3a304412b407950112b4095b0601e3&fileId=db3a304412b407950112b433b63c5d4d](http://www.infineon.com/dgdl/DS_FF300R12KE3_3_2.PDF?folderId=db3a304412b407950112b4095b0601e3&fileId=db3a304412b407950112b433b63c5d4d).
  - [30] Datasheet for SKM300GM12T4, Rev. 0 - 22.06.2009. Retrieved from [http://www.semikron.com/products/data/cur/assets/SKM300GM12T4\\_22892480.pdf](http://www.semikron.com/products/data/cur/assets/SKM300GM12T4_22892480.pdf).
  - [31] Datasheet for MII300-12A4, 20090812a. Retrieved from [http://ixapps.ixys.com/DataSheet/MI300-12A4\\_MID300-12A4\\_MDI300-12A4.pdf](http://ixapps.ixys.com/DataSheet/MI300-12A4_MID300-12A4_MDI300-12A4.pdf).
  - [32] A.M. Trzynadlowski, Control of Induction Motors, Academic Press, CA, 2001.